Highly Resolved MR Imaging of Arbitrary Subregions in Large Objects by a Whole-Body Imager

Karin Pfeffer, Markus Pfeffer, Wulf-Ingo Jung, Otto Lutz, and Fritz Schick
Institute of Physics, University of Tübingen, Tübingen, Germany

Z. Naturforsch. **48a**, 753–758 (1993); received April 17, 1993

Highly resolved images of defined regions of interest within extended objects were obtaind with a 1.5 T whole-bode imager and standard hardware. The high-resolution spin echo imaging sequence avoids aliasing and allows pixel resolutions down to 39 μm which are confirmed by phantom measurements. The application of the sequence to large biological objects such as, for example, an amaryllis bulb results in images which provide much detail which could not be resolved with standard sequences.

Introduction

Magnetic resonance imaging of biological objects provides insight into morphological and functional properties without causing destruction of the organisms. Small objects up to the size of e.g. a rat can be investigated in microscopic units with high spatial resolution. Large objects must be examined using whole-body imagers designed for medical applications. Such whole-body magnetic resonance scanners are constructed to image objects with dimensions of up to 50 cm in diameter.

If a 256 square matrix is used to represent a field of view (FOV) of 500 mm × 500 mm, FOV 500 mm, the pixel resolution is 1.95 mm. The pixel resolution depends on the integral of the gradient over time. The spatial resolution can be increased by increasing the gradient strengths until the hardware limit of the imager is reached. Further improvement of the resolution is only obtained by increasing the duration of the gradients. However, signals from the periphery of the region of interest (ROI) are in this case folded back into the image using standard imaging techniques. Furthermore, by increasing the gradient integrals only images with a fixed center can be obtained, where the center is defined by the point in the 2 D space where the influence of the gradient is zero. To avoid aliasing different approaches exist: one is simply to use a volume restriction determined by the sensitivity of the rf-coil, e.g. using a surface coil, e.g. [1, 2]. An other method is to saturate the signals from the area surrounding the ROI [3–6] or to perform a selective excitation of the ROI only [7–12].

We report on a high-resolution imaging method which permits observation of a ROI at arbitrary positions within an extended object with a commercial whole-body imager without hardware change. Small surface coils are not necessary.

Reprint requests to Prof. Dr. Otto Lutz, Physikalisches Institut der Universität Tübingen, Auf der Morgenstelle 14, 72076 Tübingen, Germany.

Method

The high-resolution spin echo sequence is shown in Figure 1 a. The 90° pulse selects the slice to be imaged. Directly after the 90° pulse the phase encoding gradient (gradient 3) is switched. To avoid folded signals from outside the volume of interest, a 180° selective pulse inverts the magnetization within a broad stripe orthogonal to the excited slice. Therefore the spin echo signal only stems from the intersection of the excited slice and the inverted stripe, i.e. two dimensions of the desired ROI are selected. The restriction in the third direction is obtained during the readout time by the receiver lowpass filter. The lowpass filter eliminates all signal components outside the desired region. This concept of aliasing-free imaging is schematically illustrated in Figure 1 b.

However, there is only one frequency to be varied in the whole-body imager. This frequency constitutes the carrier frequency of the transmitted pulses, serves as the reference frequency for the receiver, and determines the center of the frequency band selected by the lowpass filter. Thus, to select an ROI in readout direction the frequency must be changed. Changing the frequency results in a shift of the origin of the coordi-

0932-0784 / 93 / 0700-0753 $ 01.30/0. – Please order a reprint rather than making your own copy.

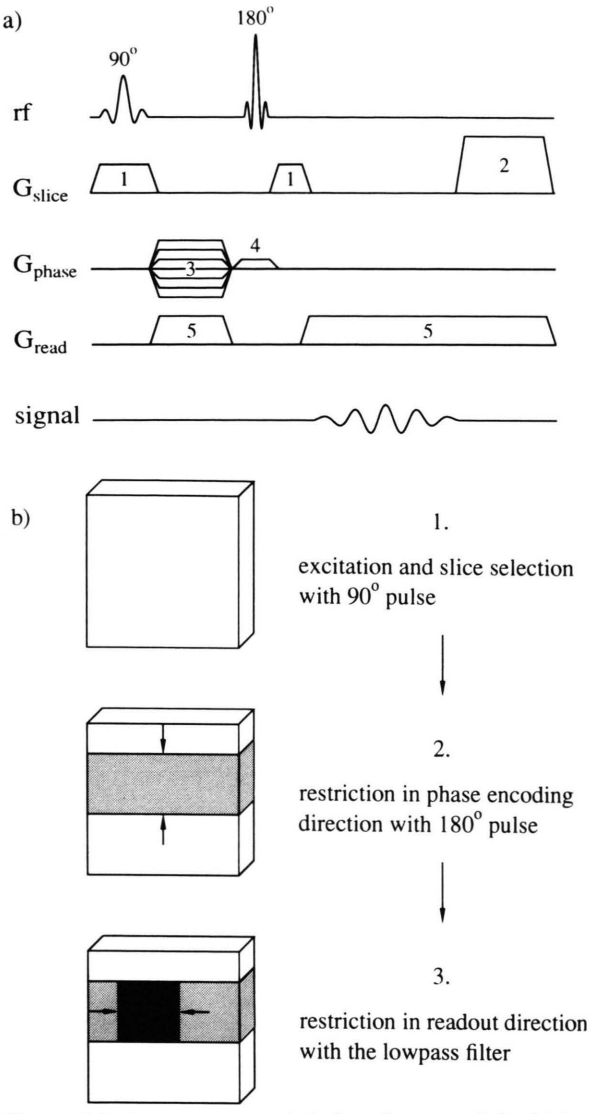

Fig. 1. a) Pulse sequence and timing diagram of the high-resolution and aliasing-free sequence. Both rf-pulses are Hamming filtered sinc-pulses. For a 40 mm FOV, the minimum echo time is 27 ms, the minimum repetition time 50 ms. b) Schematic representation of the aliasing free imaging technique.

nate system on which the sequence parameters are based, in all three dimensions. The pulse envelopes of the 90° and 180° pulses must be altered to compensate for the frequency shift appropriate to the strength of the particular slice selection gradient. It should be noted that in some cases the lines of pixels in phase encoding direction must be scrolled in the calculated image on the screen, depending on the chosen ROI and FOV.

Table 1. Comparison of high-resolution sequences and the standard spin echo sequence with a FOV of 83 mm.

FOV[a]/mm	40	20	10	83 (SE)
TE/ms	27	43	74	15
TR/ms	50	74	120	35
Phase encoding time/ms	7.68	15.36	30.72	3.84
Readout time/ms	15.36	30.72	61.44	7.68
Pixel resolution[a]/μm	156	78	39	324[b]

[a] With a 256 × 256 matrix.
[b] Assuming the dimension of the object is less than or equal to the FOV and in the center of the magnet.

Experimental and Results

All experiments were performed on a 1.5 T Siemens Magnetom whole-body imager with a maximum gradient strength of $10 \cdot 10^{-3}$ T/m. The matrix size for all images was set to 256 × 256. The smallest FOV, achieved with a standard spin echo sequence from the manufacturer using maximum gradient strength, is 83 mm, resulting in a pixel size of 0.32 mm × 0.32 mm.

The high-resolution spin echo sequence shown in Fig. 1a provides a FOV down to 10 mm. The 90° pulse has a length of 5.12 ms so as to get a good slice profile for thin slices. It is followed by the 2.56 ms rephasing pulse with 180° flip angle. For a FOV of 40 mm the phase encoding gradient has a length of 7.68 ms and the readout time is set at 15.36 ms. Gradient 2 and the prolongation of the readout gradient 5 serve as spoil gradients.

Different phantoms [13] have been used to test the sequences for different FOV's. To demonstrate the high spatial resolution, Fig. 2 shows an image of a phantom used to determine the resolution quality of sequences (top left). It consists of a polymethylmethacrylate (PMMA) cylinder (outer diameter 200 mm) filled with an isotonic solution of NaCl and with different inserts made of PMMA. As ROI, the part marked with the square was selected (zoomed by software on the top right). A high-resolution image of this region obtained with the 40 mm FOV sequence is shown on the bottom left of Figure 2. The bar on the right indicates 1 cm. On the bottom right a part of the high-resolution image is magnified by software after recording the image. The two PMMA bars with a length of 160 mm and a breadth of 5 mm form an angle of 2.1°. The wedges are clearly resolved up to a distance of 2 mm from the apex corresponding to a

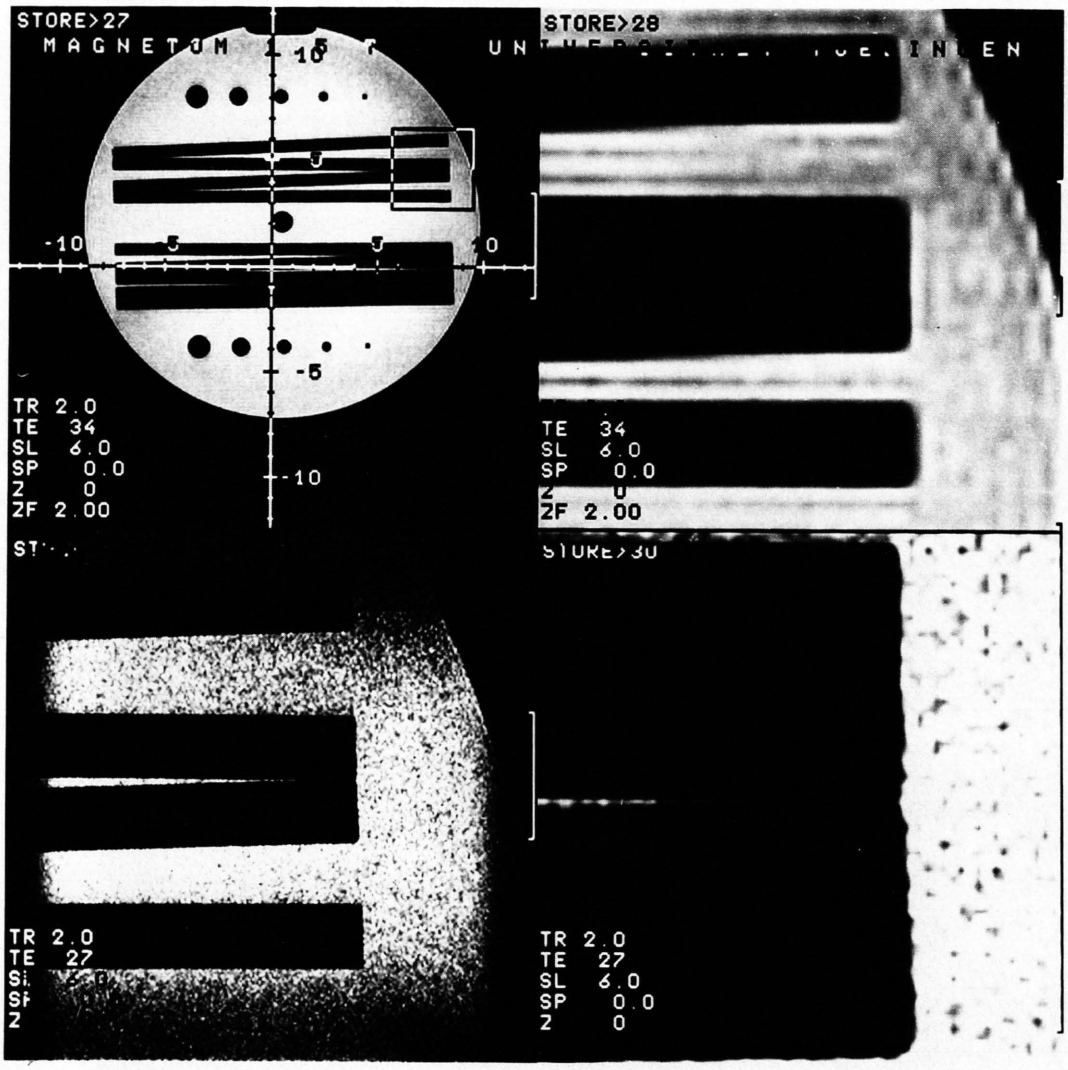

Fig. 2. *Top left:* Image of the bodycoil phantom with a FOV of 250 mm; *top right:* magnified image of the region of interest marked by the square in the overview image. Experimental data: TR = 2 s, TE = 34 ms, slice thickness 6 mm, 1 acquisition, measuring time 8.5 min; *bottom left:* high-resolution image taken with the 40 mm FOV sequence (the bar on the right indicates 1 cm); *bottom right:* a part of the high-resolution image zoomed by software. Experimental data: TR = 2 s, TE = 27 ms, slice thickness 6 mm, 8 acquisitions, measuring time 68 min.

gap of 75 μm between the bars. It should be mentioned that the phantom was situated in the bodycoil.

Three high-resolution sequences were developed with different properties with regard to the minimal echo time (TE) and pixel resolution. The properties of the sequences are summarized in Table 1 in comparison with a standard spin echo sequence of the manufacturer. The minimum FOV of the different high-resolution sequences are demonstrated in Figure 3. On the top left an overview image with a standard gradient echo sequence shows the phantom which was filled with $CuSO_4$ doped water. In this case the headcoil of the imager was used. The steps of the stairs to be imaged with the high-resolution sequences are 5 mm long and 2 mm high. The FOV's are: 40 mm (top right), 20 mm (bottom left), and 10 mm (bottom right). The corresponding pixel sizes with the 256 square matrix used were 156 μm × 156 μm, 78 μm × 78 μm,

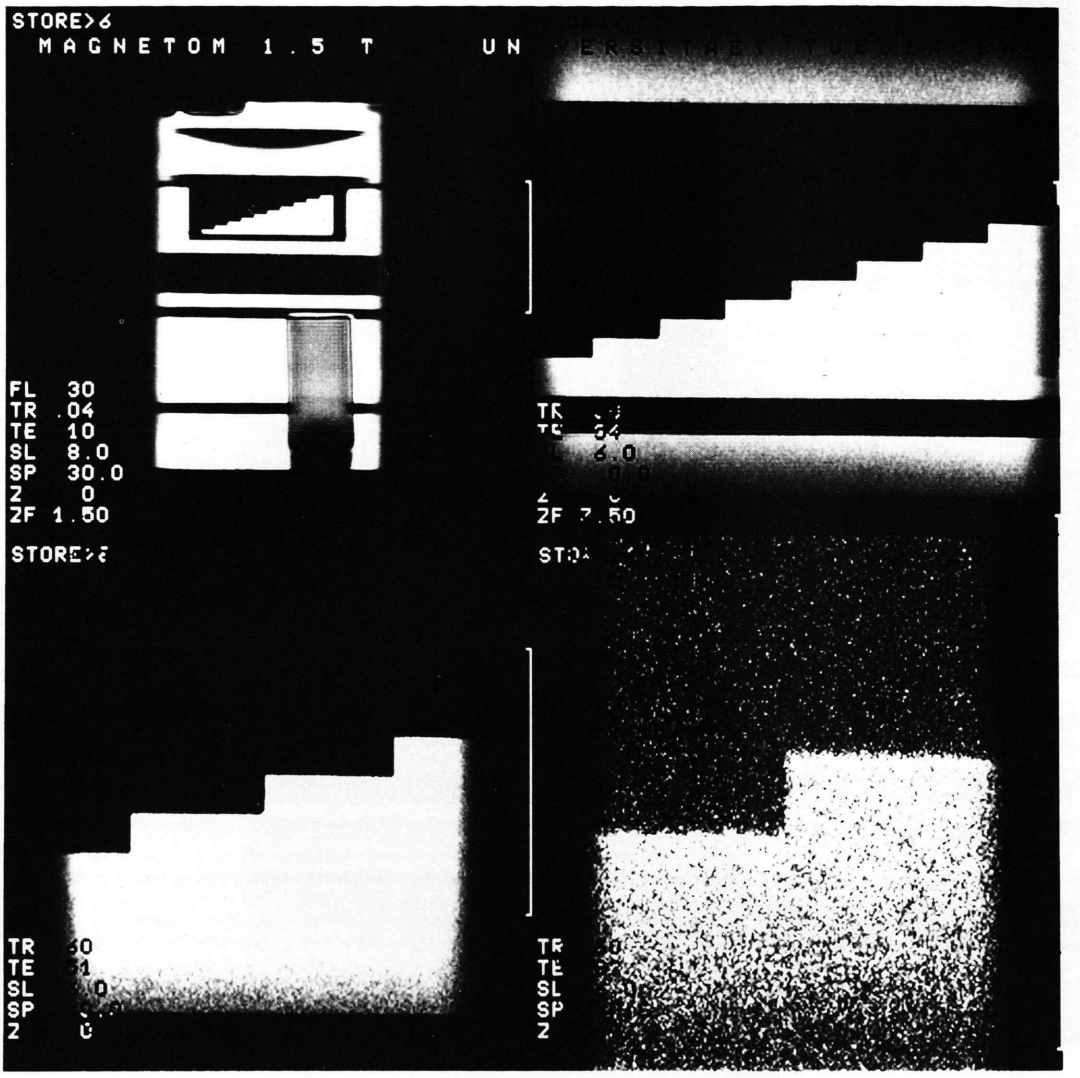

Fig. 3. *Top left:* Overview image of the phantom used. One step of the stairs has a length of 5 mm and a height of 2 mm; *top right:* FOV of 40 mm; *bottom left:* FOV of 20 mm; *bottom right:* FOV of 10 mm. TE = 34 ms, 51 ms, and 82 ms, respectively, 256 × 256 matrix, TR = 0.6 s, 8 acquisitions, slice thickness 6 mm, measuring time 21 min.

and 39 μm × 39 μm, respectively. All images were taken with 8 acquisitions. The loss in S/N due to volume reduction and echo time prolongation is obvious.

The 40 mm FOV sequence was applied to biological objects. As one example, a planted Amaryllis bulb measuring about 10 cm in diameter was examined. A fast overview image is given in Figure 4. The high-resolution image in Fig. 5 was obtained from a cross-section at slice position +72 mm (indicated with a bar in Figure 4). In the middle of the high-resolution image in Fig. 5 four fresh leaves and on the left and on the right growing blossoms can be seen with four flower buds each. The pixel resolution in this image is 156 μm × 156 μm, the slice thickness is 1.5 mm. The structures with high signal intensity in the leaves have a distance of around 850 μm. Although some resolution loss occurs due to partial volume effects this image is of high quality and reflects the usefulness of the method for biological applications.

Further prolongation of the phase encoding and readout time to 61.44 ms and 122.88 ms, respectively, results in a sequence with only 5 mm FOV. But there

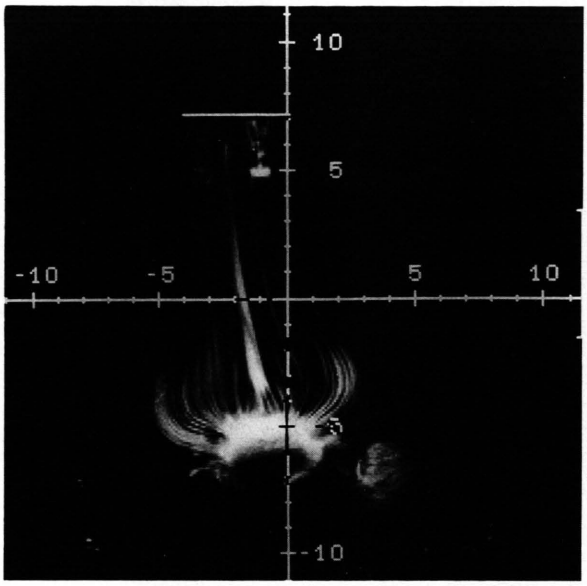

Fig. 4. Overview image of an Amaryllis bulb recorded in 10 s by a Flash-sequence. The flower pot has a diameter of 16 cm; some roots can be seen at the bottom of the image.

are severe limitations of the resolution using large receiver coils: the signal/noise ratio (S/N) [14, 15] deteriorates for smaller picture elements and the structures of the object cannot be resolved any more even if they are much larger than the pixel size. Some loss in S/N can be balanced by the number of acquisitions, e.g. for a 40 mm FOV, high-resolution images with a slice thickness of 1.5 mm and a satisfactory S/N, 16 acquisitions are necessary. This needs a measuring time of 68 min when a repetition time (TR) of 1 s is used (as in Figure 5). A FOV of 20 mm yields only 1/4 of the signal per pixel. To achieve the same S/N, the 16fold number of acquisitions and therefore the 16fold measuring time are necessary. However, the useful maximum measuring time depends on the time stability of the technical components of the imager [16, 17].

Dependent on the properties of the sample other limitations may occur: molecular diffusion [18–25], which is the main resolution limit in high field microscopy, partial volume effects [26] as already mentioned, and the natural linewidth of the substances [16, 27–31] can worsen the resolution obtained. Some further resolution limiting effects are distortions through changes in magnetic susceptibility [32–35] and displacement through chemical shift [16].

In conclusion, it has been shown that sequences with a small FOV and high resolution can be successfully applied on whole-body imagers. The application of the 180° rephasing pulse in presence of a gradient in phase encoding direction completely avoids aliasing problems. It was shown that arbitrary ROI's in large objects can be selected and imaged. So the advantage of a whole-body imager in imaging large objects is connected with the ability to obtain highly resolved images. The method is only applicable for sequences with more than one rf pulse, e.g. spin echo sequences. Prolonged measuring times of more than an hour must be allowed for in order to obtain a suitable S/N in images with high resolution better than 0.1 mm.

Acknowledgement

Financial support by the Deutsche Forschungsgemeinschaft and the Bundesminister für Forschung und Technologie (BMFT) of the Federal Republic of Germany (Grant 01 VF 85184) is gratefully acknowledged. We thank Siemens Medizintechnik, Erlangen, for technical support.

[1] D. J. Huber, R. Sauter, E. Müller, H. Requardt, and H. Weber, Radiology **158,** 405 (1986).
[2] T. K. F. Foo, F. G. Shellock, C. E. Hayes, J. F. Schenck, and B. E. Slayman, Radiology **183,** 277 (1992).
[3] U. Klose, Medizinische Physik (H. Bergmann, ed.), 476 (1987).
[4] R. R. Edelman, D. J. Atkinson, M. S. Silver, F. L. Loaiza, and W. S. Warren, Radiology **166,** 231 (1988).
[5] H. König, U. Klose, S. Sell, R. Klier, and K. Küper, Fortschr. Röntgenstr. **150,** 205 (1989).
[6] A. J. S. De Crespigny, T. A. Carpenter, and L. D. Hall, J. Mag. Res. **88,** 406 (1990).
[7] A. A. Maudsley, J. Magn. Reson. **41,** 112 (1980).
[8] R. Mezrich, L. Axel, L. Dougherty, and H. Y. Kressel, Fourth Annual Meeting of the SMRM, Aug. 19–23, 1985, London, p. 1030.
[9] D. A. Feinberg, J. C. Hoenninger, L. E. Crooks, L. Kaufmann, J. C. Watts, and M. Arakawa, Radiology **156,** 743 (1985).
[10] T. E. Conturo, R. R. Price, and A. H. Beth, Magn. Reson. Med. **6,** 418 (1988).
[11] J. Briand and L. D. Hall, J. Magn. Res. **83,** 418 (1989).
[12] J. B. Weaver, R. D. Harris, and P. K. Spiegel, Magn. Reson. Imaging **9,** 389 (1991).
[13] O. Lutz, M. Braun, and M. Pfeffer, BMFT 01 VF 85184 (1990).
[14] C. D. Eccles and P. T. Callaghan, J. Magn. Reson. **68,** 393 (1986).
[15] P. T. Callaghan and C. D. Eccles, J. Magn. Reson. **71,** 426 (1987).

Fig. 5. High-resolution image of the inner part of an Amaryllis bulb from above with growing leaves in the middle and two blossoms, recorded by the headcoil. FOV = 40 mm, pixel resolution 156 μm × 156 μm,. TE = 27 ms, TR = 1 s, slice thickness 1.5 mm, 16 acquisitions, measuring time 68 min.

[16] M. Pfeffer, W.-I. Jung, K. Müller, and H. Weissmann, Digit. Bilddiagn. **9,** 123 (1989).
[17] W. Kuhn, Angew. Chem. **102,** 1 (1990).
[18] H. Y. Carr and E. M. Purcell, Phys. Rev. **94,** 630 (1954).
[19] P. T. Callaghan and C. D. Eccles, J. Magn. Reson. **78,** 1 (1988).
[20] C. B. Ahn and Z. H. Cho, Med. Phys. **16,** 22 (1989).
[21] B. P. Hills, K. M. Wright, and P. S. Belton, Magn. Reson. Imag. **8,** 755 (1990).
[22] W. B. Hyslop and P. C. Lauterbur, J. Magn. Reson. **94,** 501 (1991).
[23] C. B. Ahn and Z. H. Cho, Magn. Reson. Med. **19,** 228 (1991).
[24] B. Pütz, D. Barsky, and K. Schulten, J. Magn. Reson. **97,** 27 (1992).
[25] E. W. McFarland, Magn. Reson. Imag. **10,** 269 (1992).
[26] F. W. Wehrli, D. Shaw, and J. B. Kneeland, Biomedical Magnetic Resonance Imaging, VCH, Weinheim 1988.
[27] W. V. House, IEEE Trans. Nucl. Sci. **NS-31,** 570 (1984).
[28] Z. H. Cho, C. B. Ahn, S. C. Juh, H. K. Lee, R. E. Jacobs, S. Lee, J. H. Yi, and J. M. Jo, Med. Phys. **15,** 815 (1988).
[29] J. M. Pope and V. Sarafis, Chem. Australia **1990,** 221.
[30] Z. H. Cho, C. B. Ahn, S. C. Juh, R. M. Friedenberg, R. E. Jacobs, and S. E. Fraser, J. Vis. Com. Imag. Represent. **1,** 56 (1990).
[31] S. Sykora, Magn. Reson. Imag. **9,** 833 (1991).
[32] K. M. Lüdeke, P. Röschmann, and R. Tischler, Magn. Reson. Imag. **3,** 329 (1985).
[33] D. T. Edmonds and M. R. Wormald, J. Magn. Reson. **77,** 223 (1988).
[34] P. T. Callaghan, J. Magn. Reson. **87,** 304 (1990).
[35] S. Posse and W. P. Aue, J. Magn. Reson. **88,** 473 (1990).